Melting of gold clusters

C. L. Cleveland, W. D. Luedtke, and Uzi Landman

School of Physics, Georgia Institute of Technology, Atlanta, Georgia 30332-0430

(Received 3 February 1999)

Investigations of the thermal evolution of structural and dynamic properties of gold nanocrystalline clusters of variable size (Au_{75}, Au_{146}, and Au_{459}) were performed using extensive molecular-dynamics simulations employing embedded-atom interactions. These studies reveal that the thermal evolution of these clusters is punctuated by diffusionless solid-to-solid structural transformations from the low-temperature optimal structures (truncated-decahedra for Au_{75} and Au_{146}, and a face-centered-cubic structure with a truncated-octahedral morphology for Au_{459}) to icosahedral structures. These structural transformations are precursors to the melting transitions which occur at temperatures below the bulk melting temperature of crystalline gold, and they are intrinsic to the thermodynamics of the clusters. The melting scenario revealed by the simulations for these gold clusters differs from that involving thickening of a quasiliquid wetting surface layer, and in addition it does not involve at any stage of the thermal process dynamic coexistence where the cluster fluctuates between being entirely solid or liquid. For the larger cluster, Au_{459}, a thermodynamic (icosahedral) solid-liquid coexistence state is found in the vicinity of the melting transition. The occurrence of polymorphic solid structures, that is a cluster containing simultaneously decahedral and icosahedral parts, is discussed in light of early observations of such structures via high-resolution electron microscopy. [S0163-1829(99)16231-3]

I. INTRODUCTION

Melting of material clusters is a subject that has been studied theoretically and experimentally for a rather long time. Indeed, the decrease of the melting temperature of small materials aggregates with reduction of their size, discussed as early as 1871 by Lord Rayleigh,[1] has been observed and studied rather extensively,[2–21] and issues pertaining to the nature of the melting process and the existence and properties of equilibrium phase coexistence in finite systems continue to be a subject of current interest.

In addition to the aforementioned reduction in melting temperature, some of the main findings about melting of clusters include the following (i) Broadening of the melting transition, and the appearance of a characteristic S-shaped loop in the caloric curve (i.e., total energy plotted vs temperature) in the transition region. (ii) The occurrence of structural isomerizations upon heating (driven by vibrational and configurational entropy considerations[4–6,8,16,22]), signified (in simulations) by changes in the slope of the caloric curve prior to melting. (iii) Surface premelting, analogous to that found in studies of heated extended surfaces.[23] (iv) Generalization of the (bulk) concept of equilibrium thermodynamic phase coexistence to include ''dynamic coexistence'' (DC) states, occurring in relatively small clusters where in the vicinity of melting an individual cluster may fluctuate in time between being entirely solid or liquid.[7,8,11] In the DC regime, which was observed in molecular-dynamics (MD) simulations, the issue of time scales is of importance, and results depend on the length of the observation time relative to the mean interval spent in the different phases and to the transit between them. Additionally, it has been shown that true solid-melt phase coexistence may occur in sufficiently large clusters,[8,14] and the nature of such states (that is nonwetting, partial wetting, and complete wetting geometries) has been explored. (v) Recent experimental observations[18,21]

of nonmonotonic dependence on size (i.e., number of atoms) of the melting temperature of sodium clusters, suggesting possible correlation with cluster ''magic number sequences'' (that is enhanced stability of clusters of particular sizes, originating from electronic shell effects and/or atomic geometric packing arrangements). (vi) The occurrence of icosahedral precursors to melting of gold clusters, revealed via MD simulations, where at elevated temperatures the melting process was found to be punctuated by solid-to-solid structural transformations to icosahedral structures.[20]

In this paper we focus mainly on the issue of structural transformations [(vi) above], through MD studies of gold clusters of increasing size: Au_{75}, Au_{146}, and Au_{459}. These clusters belong to a (discrete) family of gold clusters, identified through theoretical and experimental investigations.[24(a)] Furthermore, comparison between theoretically predicted and experimentally measured x-ray scattering intensities established the structural evolution in this family of gold clusters.[24] Accordingly, clusters of this family in the range of 70–250 atoms (effective diameters of 1–2 nm) belong to a truncated decahedral (Dh) motif;[24(a)] in particular, the optimal (low-temperature) structure of Au_{75} and Au_{146} are Marks decahedra (m-Dh), where re-entrant (111) facets are introduced via a modified Wulff construction[16,25,26] to optimize the clusters' energetic stability through a balance between surface and strain energy contributions. Consequently, these structures (see Fig. 1) are designated as Au_{75} m-Dh (2,2,2) and Au_{146} m-Dh (3,2,2); for the meaning of the indices (m,n,p), see Fig. 1. On the other hand, larger gold clusters belonging to the above mentioned family assume face-centered-cubic (fcc) structure with a truncated-octahedral morphology (TO) and variants thereof (TO$^+$);[24(b),(c)] specifically the optimal structure of Au_{459} is a fcc crystallite with a TO$^+$ morphology (see Fig. 1).

The paper is organized as follows: pertinent details of the MD simulations and analyses are described in Sec. II. Re-
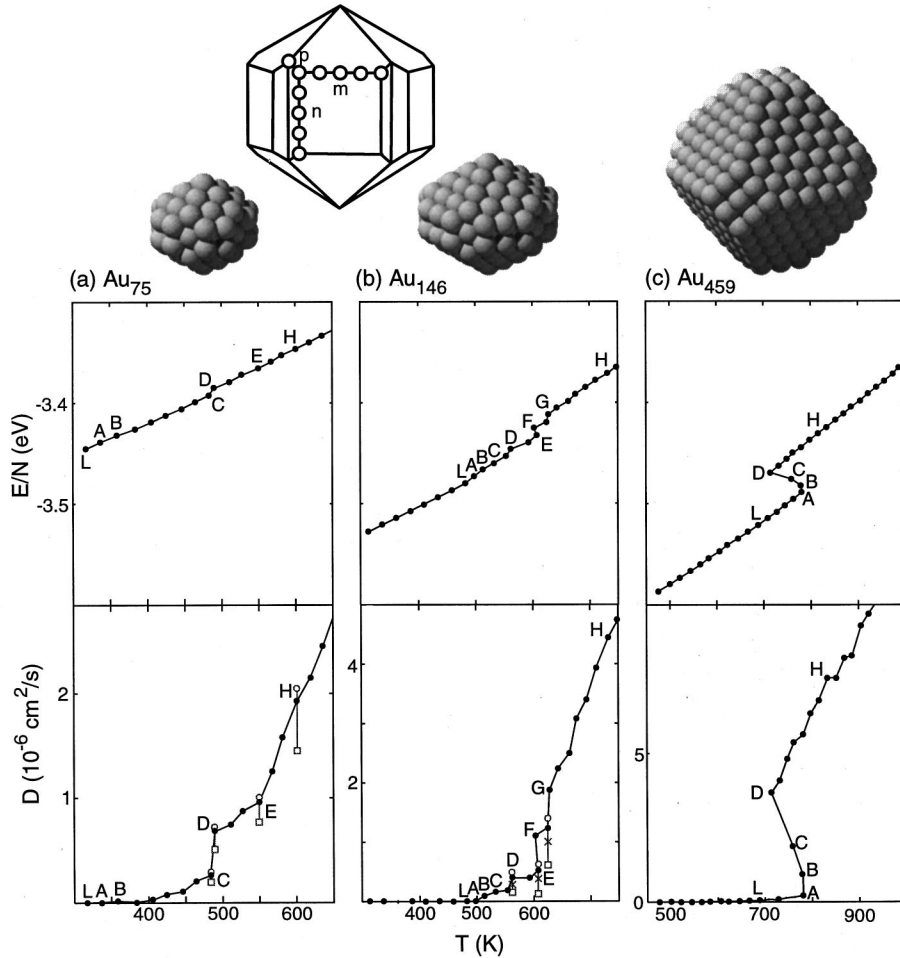
FIG. 1. Top: Energy-optimized atomistic structures of the three gold clusters studied. The two smaller clusters are Marks decahedra: (a) $Au_{75}m$-$Dh(2,2,2)$ and (b) $Au_{146}m$-$Dh(3,2,2)$, with the (m,n,p) indices as indicated in the schematic drawing. The Au_{459} cluster shown in (c) is fcc with a truncated-octahedral morphology, TO^+. For each of the clusters we display plots of the caloric curve (top panel) and diffusion constants (bottom panel) vs temperature, obtained from constant energy calculations (in the caloric curves we give the total energy per atom, E/N). (a) Au_{75}: for the diffusion constant (bottom panel), the solid dots correspond to values obtained for the whole cluster, and for points C, D, E, and H the squares and open circles correspond to diffusion constants calculated separately for atoms in the inner core region of the cluster [of radius 3.78 Å from the cluster center of mass (CM)] and in the outer shell (e.g., for atoms distanced by more than 3.78 Å from the CM), respectively. (b) Au_{146}: in the bottom panel values of the diffusion coefficients at points D and E and a point between F and G, were calculated, in addition to the total cluster (solid dots) for atoms: (i) in the inner core region of the cluster (i.e., a sphere of radius 3.85 Å about the center of mass, denoted by squares); (ii) in a shell 3.25 Å$<r<$5.85 Å denoted by crosses; and (iii) in the outer shell, $r>$5.85 Å (denoted by empty circles). (c) Au_{459}: in the bottom panel only values of the diffusion constant of the whole center are shown (solid dots). The total energy E is in units of eV, D in 10^{-6} cm^2/s, and T in K.

sults of our simulations are presented in Sec. III, and they are summarized in Sec. IV.

II. SIMULATION PROCEDURE

In our molecular-dynamics simulations we used the same embedded-atom method (EAM) many-atom interaction potentials employed by us previously in studies of the low-temperature size dependence of the structural motifs of gold clusters,[24] and in our investigation[20] of the melting of Au_{459}. In integration of the classical equations of motion we used a fifth-order Gear predictor-corrector algorithm with a time step of 3 fs.

For each cluster we started with the low-temperature energy-optimized structure (see Fig. 1), taken from the predicted[24] discrete family of optimal structures (i.e., "magic number" sequence) which has been confirmed experimentally.[24] In each case, the system, with zero angular and linear momenta and constant energy, was initially equilibrated near room temperature for 1 ns. After that period, a copy of the system was made, its energy was increased (by a fixed amount) by uniformly scaling the atomic velocities, and a new higher (constant) energy simulation was started, in parallel with continuation of the simulation of the lower-energy system. This procedure was repeated, yielding the caloric curves displayed in Fig. 1. The energy increments which we used were 0.5 eV for Au_{75}, 1.0 eV for Au_{146}, and 3.0 eV for Au_{459}.

In calculations of the properties of the systems, the first nanosecond of the simulations at each energy (i.e., for each mean kinetic temperature) was excluded (with even larger initial periods excluded as needed, particularly near transi-
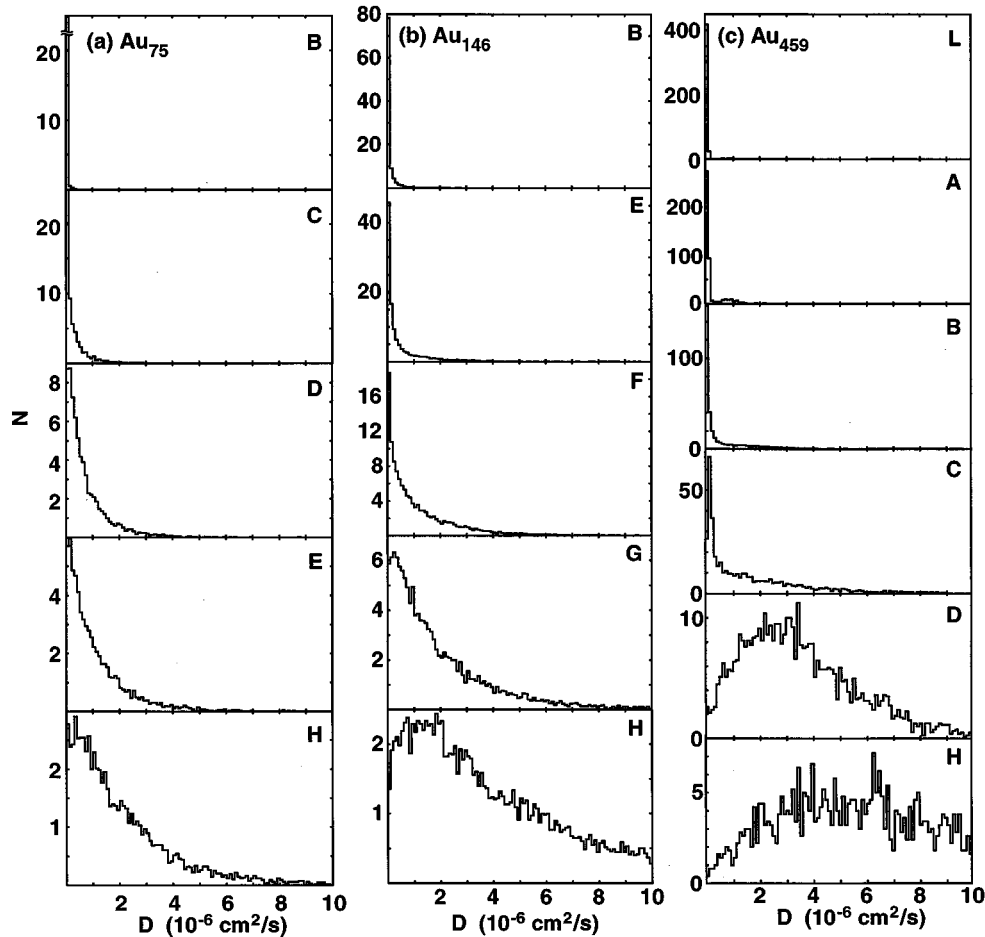
FIG. 2. Atomic diffusion coefficient (Ref. 27) histograms for the three gold clusters, calculated at the lettered points, corresponding to those indicated in Fig. 1. D is in units of 10^{-6} cm^2/s.

tion regions). Globally time-averaged properties (such as kinetic temperatures, radial distributions, and structure factors) were averaged for at least 1 ns, and for much longer times in the vicinity of transition regions where fluctuations are more pronounced. Dynamic properties, such as an individual atom's potential energy, its diffusion, or its position (the latter for use in common neighbor analysis calculations, see Appendix A) were averaged over 30 ps.

III. RESULTS

In this section we present the results of our simulations for three gold cluster sizes, Au$_{75}$, Au$_{146}$, and Au$_{459}$. To facilitate comparisons between the three cases we have chosen, when possible, to display our results in a "parallel" manner, that is, group together the analysis pertaining to a given property for the three systems. Our discussion focuses first (Sec. III A) on caloric evolution of the clusters (caloric curves, diffusion, and fluctuations), turning then to a detailed analysis of structural aspects of the thermal process (Sec. III B).

A. Caloric curves, diffusion, and fluctuations

In Figs. 1(a)–1(c), corresponding to Au$_{75}$, Au$_{146}$, and Au$_{459}$, respectively, we display at the top the caloric curves, that is the total energy per atom E/N of the cluster, plotted

versus the mean kinetic temperature $k_B T = [2/(3N - 6)]\langle \Sigma_{i=1}^{N}(m v_i^2/2)\rangle$, where the angular brackets denote averaging over time (typically 1–3 ns), and k_B is the Boltzmann constant. At the bottom panel of each figure we show, plotted vs T, the corresponding diffusion coefficient D, evaluated for each temperature as the slope of $\bar{R^2}(t)/6 \equiv (1/6)\langle\langle \Sigma_{i=1}^{N}|r_i(t) - r_i(0)|^2\rangle\rangle$, where $r_i(t)$ is the vector position of the ith atom, and the averaging denoted by the double angular brackets performed over both the atoms in the cluster and over time origins. We also include in the bottom panels the diffusion coefficients at selected temperatures, calculated for atoms assigned to different regions in the cluster (see below).

In all cases the caloric curves exhibit the following behavior: (i) a linear increase of the energy with temperature at the low- and high-temperature regimes, and (ii) pronounced changes ("breaks") in slope [see intervals CD, $DEFG$, and $ABCD$ in Figs. 1(a), 1(b), and 1(c), respectively], as well as smaller features for the two smaller clusters [see AB in Fig. 1(a) and LA in Fig. 1(b)]. These breaks in the slopes of the caloric curves correlate with discontinuities in the corresponding calculated diffusion coefficients, indicating that most likely they signify the occurrence of structural and/or (at least, partial) phase transformations (see below). As we discuss below melting of the clusters occurs in the vicinities of the points marked E, G, and C on the caloric curves in
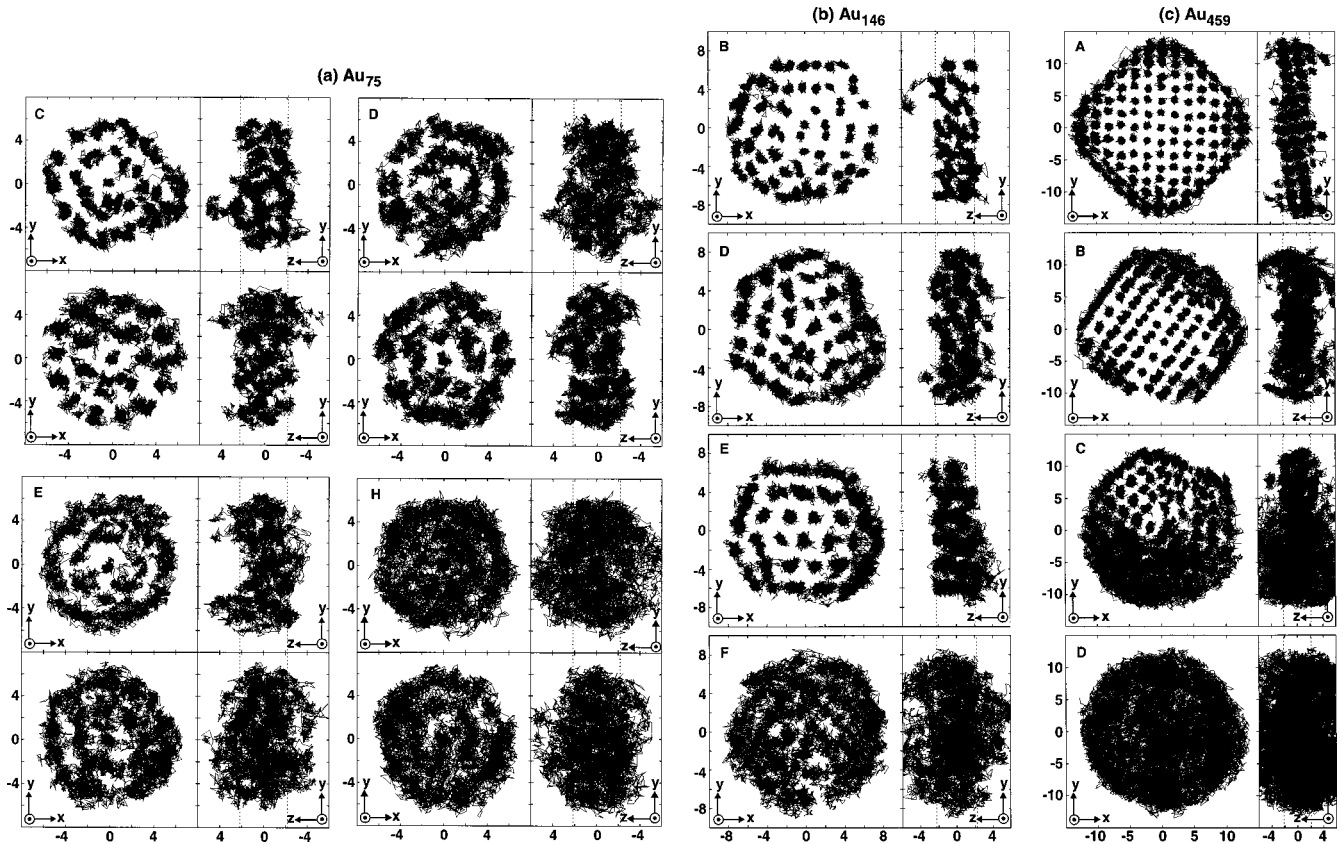
FIG. 3. (a) Au$_{75}$ trajectory plots for atoms in a 4-Å-thick slice through the cluster, centered about the center of mass of the cluster, calculated after equilibration of the cluster. Trajectories are shown for points C, D, E, and H (see Fig. 1). In each case the upper two trajectories and bottom ones were calculated (each) for time spans of 300 ps with the two time intervals separated by 800 ps. This allows one to visually estimate temporal changes (or lack thereof) in the cluster behavior during the constant energy simulations at these selected points. In each case the trajectory on the left is projected onto the (x,y) plane, and the one on the right is projected onto the (y,z) plane; spreading (larger width along the z axis) of the trajectories projected on the (y,z) axis indicates enhanced atomic diffusion. The values on the axis of the trajectory plots are distances in units of Å. (b) and (c) Same as (a), but for the Au$_{146}$ [in (b)] and Au$_{459}$ [in (c)] clusters. Here for the selected stages (indicated by letters, see also Fig. 1) we display only one 300-ps trajectory, viewed in each case in the (x,y) and (y,z) planes.

Figs. 1(a–c), respectively, that is $T(75) \sim 550$ K, $T(146)$ ~ 625 K, and $T(459) \sim 760$ K.

Added information pertaining to the degree of atomic diffusion[27] in the clusters, is given in Figs. 2(a)–2(c) where histograms of the atomic diffusion coefficients are shown for selected stages [corresponding to lettered points marked on the corresponding caloric curves, Figs. 1(a)–1(c)]. From these histograms, in conjunction with the corresponding trajectory plots shown in Figs. 3(a)–3(c) we observe the following.

(a) For the Au$_{75}$ cluster [Figs. 2(a) and 3(a)], the diffusion of atoms up to (and including) the temperature corresponding to point C[~ 480 K; see also Fig. 1(a)] is very small. The diffusion is markedly increased upon increasing the mean kinetic temperature ($T \sim 485$ K, point D) and grows gradually in the interval DE (485 K$\leq T \leq$550 K). Note, however, that throughout this interval the diffusion remains rather limited. Furthermore, one may distinguish concentric atomic shells in the heated cluster, and the diffusion occurs mainly within these shells with limited atomic transport between them. For temperatures above $T(E) \sim 550$ K, the diffusion grows linearly with temperature at a significant rate (note the break in the slope of the diffusion coefficient at point E [Fig. 1(a)]) and the diffusive motion becomes isotropic with the

diffusive atomic trajectories encompassing the whole cluster [see point H in Fig. 3(a)]. It is also of interest to note here that overall the evolution of the atomic diffusive motion with increasing temperatures does not seem to initiate predominantly at the surface of the cluster, although (particularly at lower temperatures) a small number of atoms (particularly vertex and edge atoms) may be preferentially mobile on the surface. Note here that even after the melting transition the diffusion constant of atoms in the inner part of the cluster is smaller than that of atoms in the outer shell [compare the values marked by the square and empty circle for point H in Fig. 1(a)].

(b) For the Au$_{146}$ cluster [Figs. 2(b) and 3(b)] the increase in the atomic diffusion is localized to the surface region up to point E [$T(E) = 610$ K, see Fig. 1(b)], with a marked increase upon transition from E to F (near 610 K), where in the latter state atoms at both the surface and the interior of the cluster exhibit enhanced diffusive dynamics.

(c) For the largest cluster, Au$_{459}$ [Figs. 2(c) and 3(c)], we observe limited diffusive motion, localized to the surface region up to point B. However, in contrast to the smaller clusters, a further increment in the cluster's total energy is accompanied by partial melting of the clusters, resulting in a coexistence state with an interface between part of the cluster
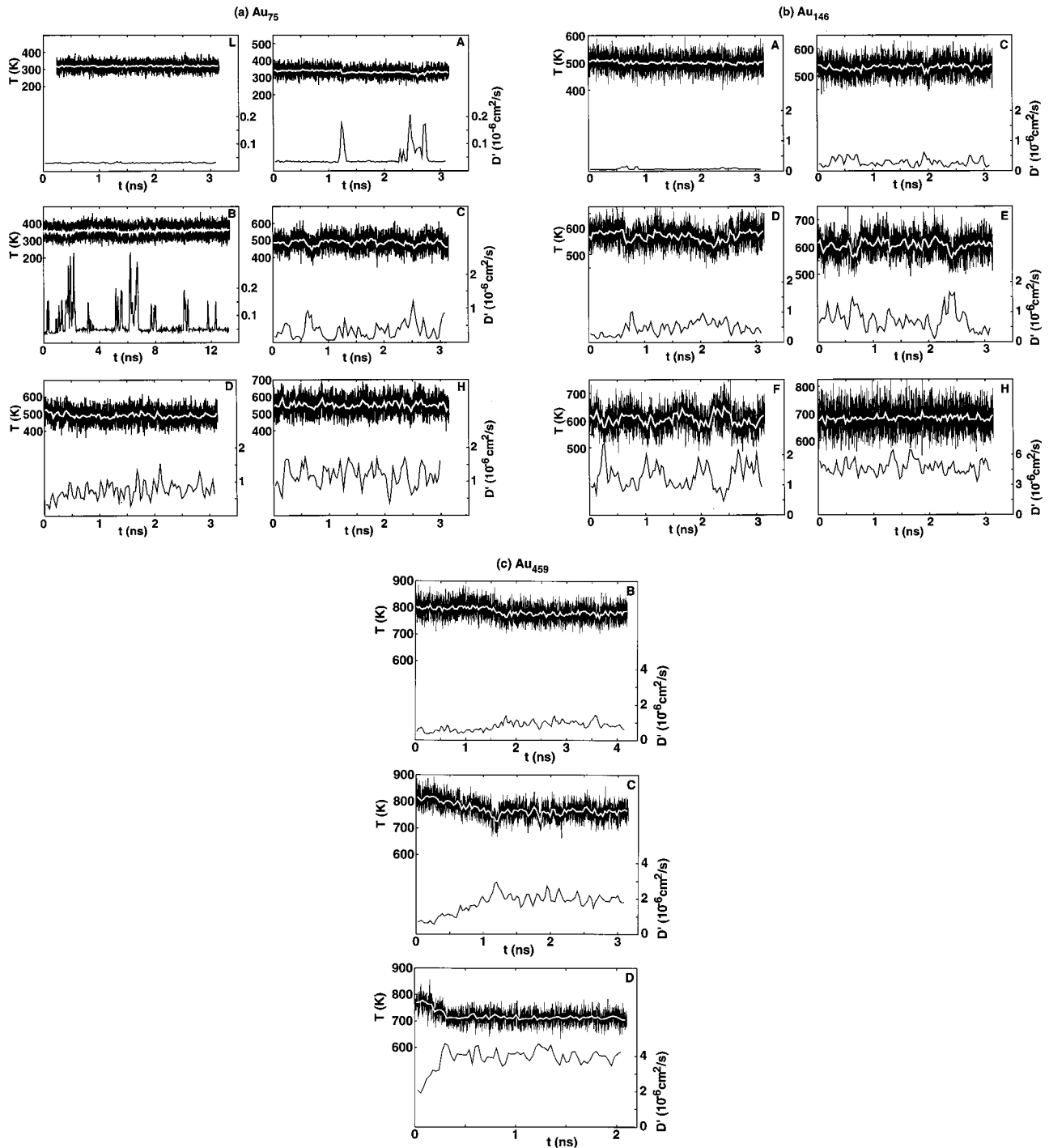
FIG. 4. (a) Au$_{75}$ cluster. Time evolutions of the kinetic temperature (T, left scale) and estimated diffusion constant D' (right scale) at various stages indicated by letters (see Fig. 1). In each case, the temperatures are displayed for points along the trajectory separated by 60 fs, with the white traces corresponding to 30-ps averages. The diffusion constants D' where estimated (using the same 30-ps time intervals) from the slope of the line connecting the beginning and end points of $R^2(t)$ (see text), and averaged over particles and time origins. Note the changes in scale of D' (on the right axes). Temperature is in K, and D' in 10^{-6} cm^2/s. (b) Same as in (a) but for Au$_{146}$. (c) Same as in (a) but for Au$_{459}$. Note the change in T and D' at stage B, occurring at ~1.6 ns and corresponding to a partial surface melting of the cluster. The decrease in T and increase of D' at stage C, occurring at $t \lesssim 1$ ns, correspond to the partial structural transformation of the cluster, and the changes in T and D' at stage D for $t \lesssim 0.3$ ns correspond to melting of the cluster.

maintaining a crystalline structure and another part exhibiting liquid characteristics [see C in Fig. 3(c)]. Further increase in the energy of the cluster results in collapse of the whole cluster into a liquid droplet with a dramatic increase in the diffusion.

In this context we comment on temporal fluctuations in the clusters' kinetic energy and atomic diffusion. One of the principal observations pertaining to the thermodynamics of small clusters is the one concerning dynamic coexistence. This term pertains to temporal fluctuations between equilib-
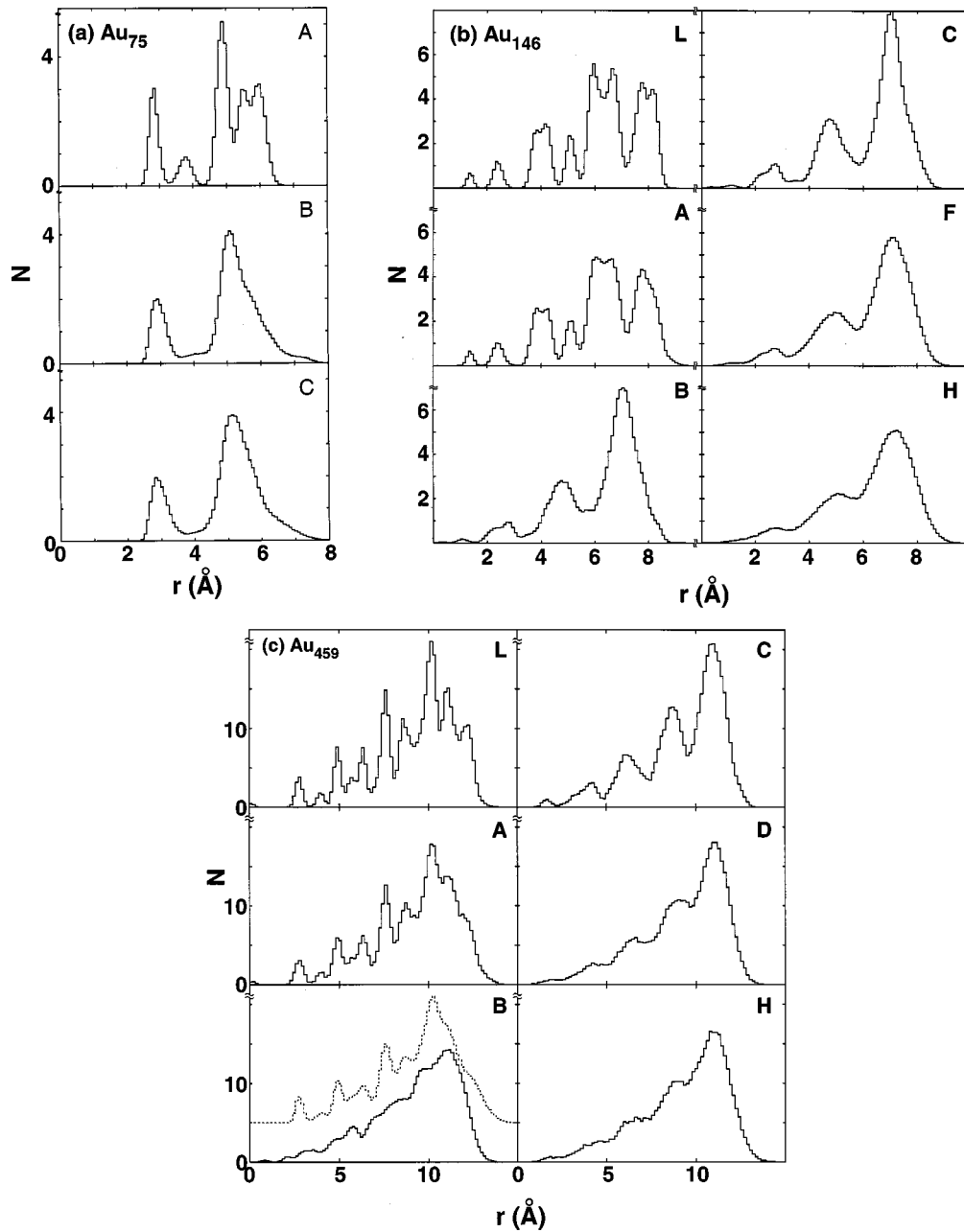
FIG. 5. (a) Au$_{75}$ cluster. Number of atoms plotted versus distance (r, in Å) from the center of mass of the cluster, displayed for the three stages indicated by letters (see Fig. 1). (b) Same as in (a) but for Au$_{146}$. (c) Same as in (a) but for Au$_{459}$. In the panel marked B the light dotted curve (shifted upwards) corresponds to calculations with the atom closest to the center of mass as the origin. This distinction does not affect the other curves.

rium states of a cluster (e.g., solid and liquid), with individual clusters transforming between being in a solid form at some time interval and in a liquid form at another; equivalently, this term refers to an ensemble with a fraction of the clusters in the ensemble being solid and the other fraction comprised of liquid clusters, but not to clusters comprised of solid and liquid parts simultaneously. To explore fluctuations in our systems in Figs. 4(a) and 4(b) we show the kinetic temperatures and diffusion coefficients D' for Au$_{75}$ and Au$_{146}$ at selected stages, plotted versus time;[27] here the kinetic temperatures and the diffusion coefficients were evaluated as short-time averages ($\Delta t \sim 30$ ps) over the simula-

tions. In both cases we observe enhanced fluctuations in the kinetic temperature and the diffusion as the total energy content of the clusters is increased; note that since in each stage of these microcanonical simulations the total energy of the cluster is conserved, an increase in the kinetic energy is accompanied by a decrease (that is a more negative value) in the potential energy, and vice versa. From these figures we observe that the fluctuations are enhanced at points corresponding to "transition stages" [that is breaks in the caloric curves, see Figs. 1(a) and 1(b)]. However, we have not detected any instances of dynamic coexistences, neither have we found at any stage solid-liquid phase coexistence for the

two smaller clusters. On the other hand the larger cluster (Au_{459}) exhibits true phase coexistence, as discussed below [see also the trajectory plot corresponding to point C in Fig. 3(c)]. The temporal fluctuations of the kinetic temperature and diffusion near the melting transition for the Au_{459} cluster are displayed in Fig. 4(c), again showing no indication of dynamic coexistence fluctuations between wholly solid and liquid forms of the cluster. The changes in the temperature and diffusion at the beginning of the time intervals, seen particularly for the stages marked C and D in Fig. 4(c), signify partial melting accompanied by a structural transformation (see below) at stage C, and completion of the melting process at stage D.

B. Structural analysis

We turn next to more detailed examinations of the evolution of structural characteristics of the clusters. In Figs. 5(a)–5(c) we display for the three clusters, at selected points marked on the corresponding caloric curves [Figs. 1(a)–1(c)], the number of atoms N plotted versus the distance from the center of mass of the cluster. From these radial atomic distributions we observe for the two smaller clusters [Figs. 5(a) and 5(b)], early obliteration of their detailed crystalline structure occurring already at rather low temperatures compared to their melting temperatures. However, we note that this loss of detail occurs at temperatures for which the atomic diffusion in the clusters is rather low. From the above, coupled with inspection of atomic configurations, we conclude that the aforementioned fluctuation patterns in Figs. 4(a) and 4(b) originate from enhanced thermal vibrational motion in the crystalline clusters (thermal softening), rather than from early liquification (premelting) of the clusters. For the larger (Au_{459}) cluster, on the other hand, we observe distinct crystalline features in the radial distributions up to the melting region [i.e., see point B in Fig. 5(c)], indicating a smaller degree of thermal enhancement of the atomic vibrational motions (particularly in the inner shells) than that observed in the smaller (less coordinated) clusters.

The type and degree of crystalline order in the clusters and their thermal evolutions are analyzed in Figs. 6(a)–6(c), where we display signatures obtained from a common neighbor analysis (CNA)[28] for selected stages of the simulations (see Appendix A). In this analysis we distinguish between signatures characteristic to a strictly fcc crystallite [denoted by $a-f$ and given left to the vertical dashed dividing line in Figs. 6(a)–6(c)], and those ($g-m$) shown to the right of the dashed dividing line, occurring only in multi-twined (decahedral or icosahedral) crystallites (here we include also Marks-decahedral structures); CNA signatures which do not belong to either of these classifications are denoted by ''?'' and are taken as corresponding to a disordered and/or melted atomic configurations. Because the structural transformations which we find involve icosahedral isomers which share similar CNA characteristics with the decahedral ones, the CNA analysis of such transformations is more complicated for the Au_{75} and Au_{146} clusters [which are of decahedral (m-Dh) morphology at low temperatures] than for the fcc truncated-octahedral Au_{459} cluster. Nevertheless, examination of Fig. 6, together with the time evolution of the CNA signatures recorded at selected stages [Figs. 7(a)–7(c)] and visual in-
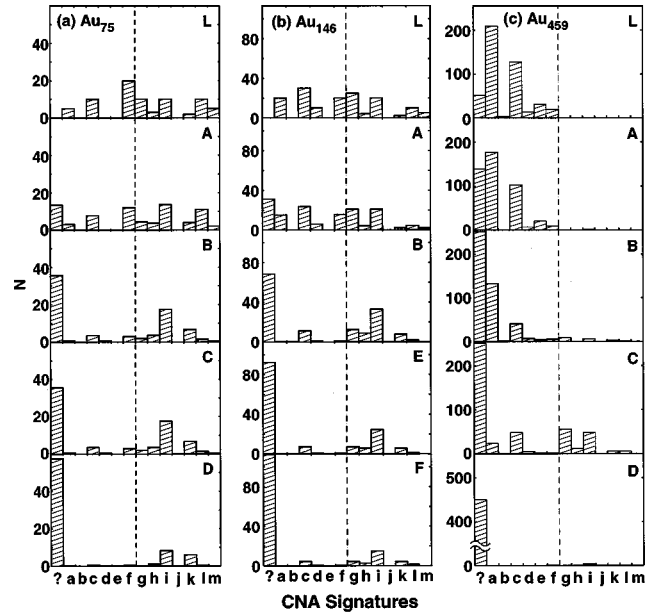

FIG. 6. Histograms of CNA signatures (see Appendix A) for the three clusters (a)–(c), at selected stages indicated by upper-case letters (see Fig. 1). The dashed vertical lines separate fcc signatures (left of the line) from icosahedral (and decahedral) signatures (right of the line). The CNA signatures (marked by letters), are explained in Table I, Appendix A.

spection of atomic configurations, allows identification of the type of structural transformations which the clusters undergo prior to melting.

From Figs. 6(a) and 7(a) we observe a marked change in the CNA characteristics of Au_{75} occurring in stage B, corresponding to $T \sim 350$ K. This change is expressed mainly by an increase in the amplitude of the indeterminate signatures (''?''), and an increase in the amplitudes of the signatures marked (i) and (k). The increase in the weight of signatures (i) and (k) indicates the emergence of icosahedral character in the cluster. Indeed, both these signatures are higher in an icosahedral structure than in a decahedral one; (i) corresponds to edges between two adjacent (111) facets, of which there are ten in an ideal decahedron and 30 in an icosahedron, and (k) corresponds to surface vertices of which there are two in a decahedron and 12 in an icosahedron. We also observe from Fig. 7(a) (stage B) the abrupt nature of the transformation (at ~ 1.5 ns). We note here that the structural transformation to a partial icosahedral isomer is signified by a small change in slope on the caloric curve [see the sequent AB in Fig. 1(a)] and is diffusionless [see Figs. 1(a) and 2(a)]. Interestingly, the (partial) icosahedral structure which emerges already at a rather low temperature maintains up to close to the melting of the cluster [point E on the caloric curve, Fig. 1(a)]. A polymorph of the Au_{75} cluster, exhibiting interfacing decahedral and icosahedral parts, recorded in stage A prior to the more complete transformation occurring in stage B, is shown in Fig. 8. Later in stage A, after formation of the polymorph the cluster completely reverts to its original decahedral form [see Fig. 7(a)], suggesting that this solid-solid transformation may reflect the existence of mechanisms by which the decahedral→icosahedral transformation can proceed in stages instead of happening every-
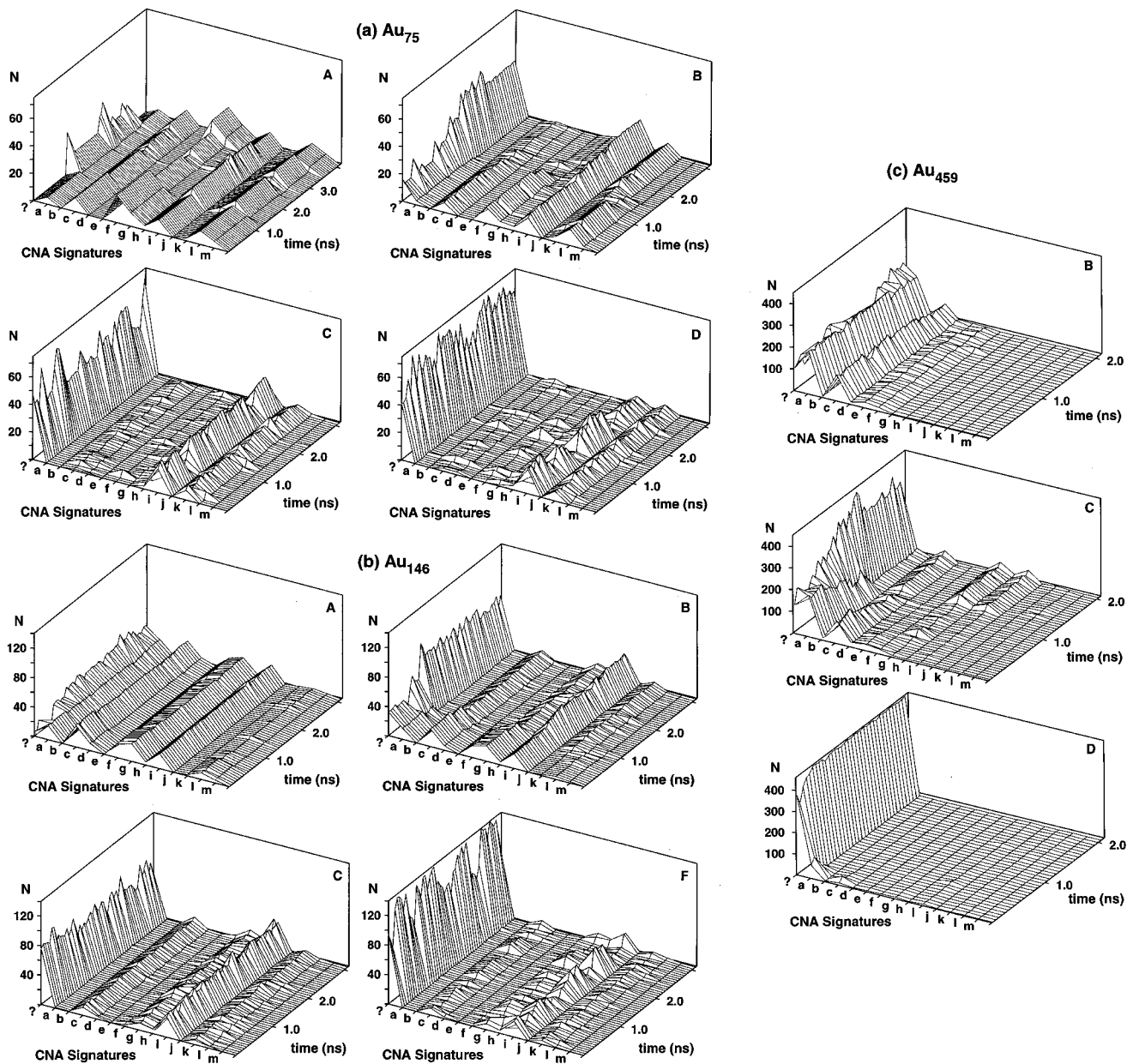
FIG. 7. (a) Au$_{75}$ cluster. Time evolutions of the CNA signatures (see Table I, Appendix A) at selected stages, indicated by letters (see Fig. 1). (b) Same as in (a) but for Au$_{146}$. (c) Same as in (a), but for Au$_{459}$.

where at once. The ability of gold to accommodate such high-strain intermediate states may underlie our observations of icosahedral precursor states during the thermal evolution of gold clusters. Similar behavior is found for the Au$_{146}$ cluster, with the $Dh \rightarrow Ih$ transformation occurring at $T \sim 510$ [see the stage marked B in Figs. 6(b) and 7(b)], although we have not isolated stable polymorphs for it.

As we noted, identification of the occurrence of icosahedral precursors to melting is easier for the large fcc-TO Au$_{459}$ cluster. Indeed, from Figs. 6(c) and 7(c) we observe the occurrence of icosahedral signatures in stage C signified particularly by the abrupt increase in the amplitudes of the CNA signatures g (corresponding to twining planes) and i. At this stage which occurs just prior to melting the (transformed) icosahedral part of the cluster coexists with a (pendant) liquid part [see the panel marked C in Fig. 3(c)].

The structural transformations discussed above, (which are driven by the vibrational and configurational entropy of the clusters at elevated temperatures[22]) are reflected in the scattering functions shown in Figs. 9(a)–9(c), calculated using the Debye formula.[29] In these plots we included the scattering intensity from ideal icosahedral structures, (of sizes close to the given clusters), equilibrated at the temperature of the transformation (see dashed lines above the solid line corresponding to the structural transformation stage). In each case the structural transformation of the cluster is signified by a change in the peak-pattern and/or line shape of the scattering function [compare the lines marked B in Figs. 9(a) and 9(b), and the line marked C in Fig. 9(c) to the scattering function traces below them, corresponding to pre-transition structures of the corresponding clusters]. We note that past the structural transformation stage (and including the com-
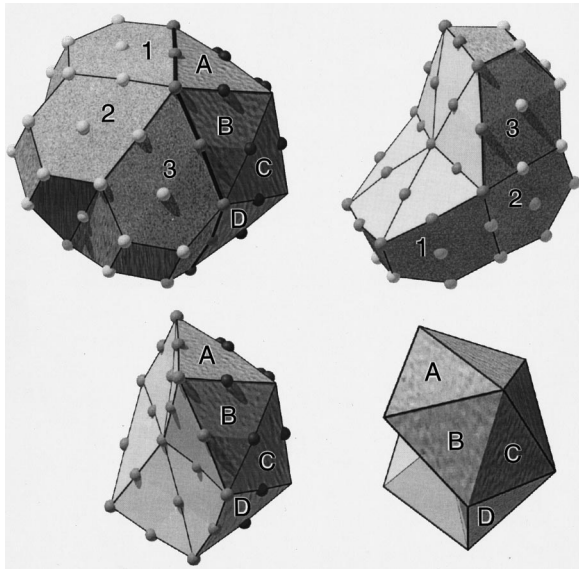
FIG. 8. Polymorph of the Au_{75} cluster, recorded during the MD simulation, exhibiting a cluster with interfacing decahedral and icosahedral parts. The polymorph occurred at ~1 ns during stage A [that is $T \sim 360$ K, see Fig. 1(a); see also Fig. 7(a), top-left frame], and the structure converted back to the decahedral one after ~2 ns [see the time dependence of the CNA signatures in Fig. 7(a)]. The decahedral part is marked by numbers (1,2,3) and the icosahedral one by letters (A,B,C). The whole polymorphic Au_{75} cluster is shown at the top left. At the bottom left we show, separately, the icosahedral part, and the decahedral part (rotated to expose the internal interface) is shown at the top right. At the bottom right we also display the piece of a perfect icosahedron corresponding to the icosahedral part (bottom left).

plete melting of the cluster), the variations in the scattering functions are rather mild and subtle.

IV. SUMMARY

In this paper we reported results of extensive molecular-dynamics simulations employing embedded-atom interactions, aimed at investigation of the melting of gold clusters of three sizes, i.e., Au_{75}, Au_{146}, and Au_{459}. At low temperatures (e.g., room temperature) these clusters are crystalline, with Au_{75} and Au_{146} having energy optimized truncated-decahedral structures, and Au_{459} being an fcc crystallite with a truncated-octahedral morphology (see Fig. 1).

The main finding of our study pertaining to the thermal evolution of these gold clusters is the occurrence of structural solid-to-solid transformations from the above low-temperature optimal structural motifs to icosahedral structures, as precursors to melting, with their eventual melting below the bulk melting temperature of gold [$T_M(\text{bulk}) = 1090$ K, calculated with the use of the same EAM interactions]; from our simulations we estimate cluster melting temperatures of $T_M(75) \sim 550$ K, $T_M(146) \sim 625$ K, and $T_M(459) \sim 760$ K [see Figs. 1(a)–1(c)]. The temperatures at which these diffusionless structural isomerization transformations occur are predicted to be ~350 K, and ~510 K for the $Dh \rightarrow Ih$ of Au_{75} and Au_{146}, respectively and ~760 K for the (fcc) $TO^+ \rightarrow Ih$ of the Au_{459} cluster (see Figs. 6 and 7). The thermal/structural evolutions of the two larger clusters
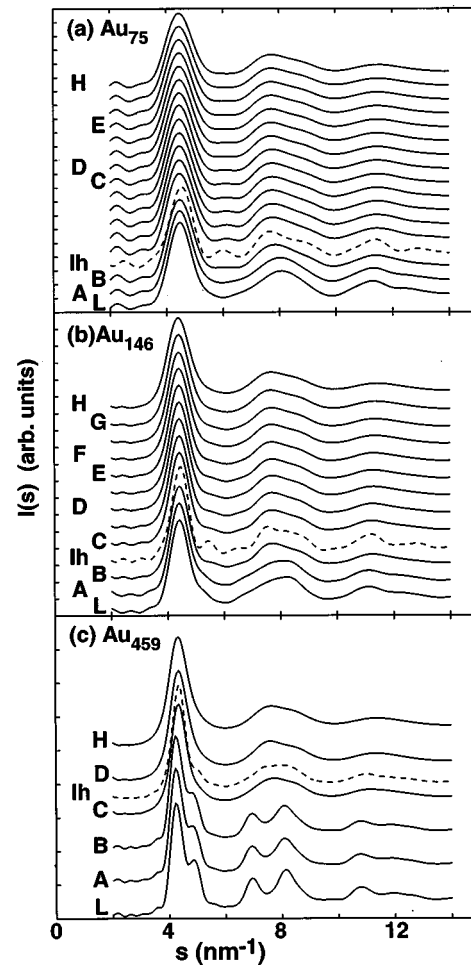

FIG. 9. Large-angle x-ray powder-diffraction intensities $I(s)$ plotted vs momentum transfer s (in nm^{-1}), for the three gold clusters. In each case $I(s)$, incorporating the atomic form factor of gold and averaged over the simulations (i.e., calculated for individual atomic equilibrium configurations evolving dynamically, and then averaged), is given for various stages corresponding to the points on the caloric curve shown in Fig. 1. The dashed line corresponds to $I(s)$ for an icosahedral cluster (of size close to that of the corresponding cluster, thermalized to the temperature of the solid line just below it).

are illustrated by the configuration/property plots shown in Fig. 10 (Au_{146}) and Fig. 11 (Au_{459}) of Appendix B, where atomistic energetic and mobility characteristics are superimposed on atomic cluster configurations recorded at selected stages of the thermal process.

The melting scenario predicted by our simulations differs from that described previously, where no such structural transformation precursors were found, and the thermal evolution involved solely surface premelting, where lower coordination and weaker bonding of surface atoms (particularly at edges and corners between surface facets) leads to thermally activated processes resulting in formation of a surface wetting quasiliquid layer at $T < T_M(\text{bulk})$. While we indeed find enhanced mobility of surface atoms at elevated temperatures, for the range of cluster sizes studied here we do not find a quasiliquid wetting layer which grows in thickness consuming eventually the whole cluster. Instead, the heating process in punctuated in these clusters by the aforementioned
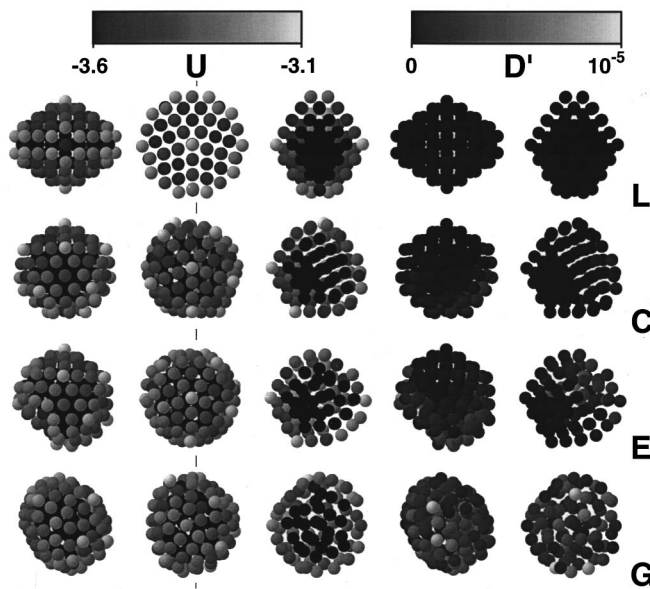
FIG. 10. Cluster configuration/property plots for Au_{146} at selected stages of its thermal evolution [L, C, E, and G; see Fig. 1(b)]. In the first three columns, configuration/energy plots are displayed [with the shading following the potential energy scale (in eV) at the top]. Configuration/diffusion plots are displayed in the fourth and fifth columns (with the scale of D in cm^2/s given at the top). The configurations in the first and fourth columns correspond to the Au_{146} cluster shown in Fig. 1 viewed along the normal to the page; that is, looking directly into a decahedral notch. The configurations in the second column correspond to a view of the cluster after a 90° rotation about x (the horizontal axis). The configurations in the third and fifth column correspond to a view obtained via cutting the cluster in the middle with a meridian (north-south) plane normal to the page (the cut line is indicated in column 2), followed by a 90° left rotation of the cluster (i.e., the plane of the cut lies in the plane of the page, allowing view of atoms in the interior of the cluster). Note the change of the shape of the cluster associated with the m-$Dh \rightarrow Ih$ structural transformation (compare configurations in the left two columns at stages L and C).

FIG. 11. Cluster configuration/property plots for Au_{459} at selected stages of its thermal evolution [L, A, B, C, and D; see Fig. 1(c)]. Configuration/energy plots (with shading following the potential energy scale, in eV, shown at the top) are displayed in the first column and configuration/diffusion plots in the two other columns. The configurations in the first and second columns correspond to a view of the Au_{459} cluster shown in Fig. 1 along a normal to the page [i.e., normal to the (100) front facet of the cluster]. The configuration on the right was obtained via the planar cut and rotation described in the caption to Fig. 10 (the cut line is indicated in the second column). An expanded color version of this figure, including the CNA signature, can be found as Fig. 2 in Ref. 20.

structural transformation into an icosahedral structure [which in the case of the larger cluster (Au_{459}) coexists with a (pendant) liquid (melted) fraction]; see the panel marked C in Fig. 3(c), culminating eventually in melting of the cluster. Additionally, we do not find any indication in our simulations for dynamical coexistence, where the whole cluster fluctuates in time between solid and liquid forms [see Figs. 4(a)–4(c)]; this is to be distinguished from the solid (icosahedral)-liquid coexistence mentioned above.

In closing, we remark that certain types of structural fluctuations in small particles have been discussed previously (Refs. 4–6; see the review in Ref. 16) in the context of high-resolution electron microscopy studies (mostly for metallic particles, such as silver and gold, larger than those treated by us here). Several models were proposed to explain such findings (that is observations that a single particle will change in time, in an apparently random manner, between a single crystal, a lamellar twin, a decahedral multi-twinned particle, or an icosahedral structure). These models include (i) the involvement of some relatively violent process (e.g., a Coulomb explosion,[30] an Auger cascade,[31] or charging[5,32]),
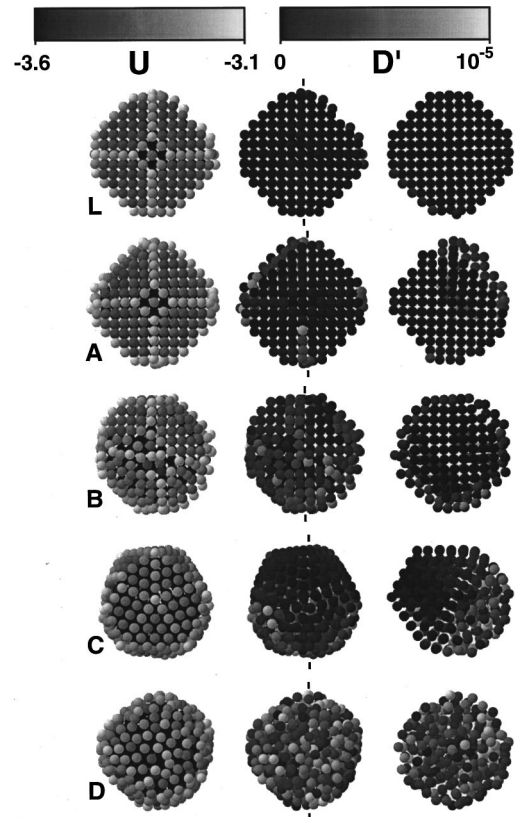
and (ii) intrinsic thermodynamic models, postulating structural coexistence associated with a relatively ''soft'' configurational energy surface,[6,16] and the effect of vibrational entropy on structural isomerization.[13] Our results support the latter models, in showing that the structural-transformations (icosahedral) precursors to the melting transition of (isolated) gold clusters, are indeed of intrinsic thermodynamic nature, rather than the results of electronic excitations, charging or other extrinsic effects, thus providing insights into the nature of phase transformations of metal particles of reduced dimensions. In this context we also note our finding pertaining to the occurrence of polymorphic particles (see Fig. 8, where a cluster made of an icosahedral and a decahedral part joined at an interface, is displayed for Au_{75}). Interestingly such polyparticles (though of a much larger size) were found via high-resolution electron microscopy,[33] where it has been suggested that indeed such configurations may correspond to local energy minima stable to small perturbations. Our finding may constitute confirmation of these early studies.

TABLE I. Atomic CNA signatures in terms of bond CNA signatures, for various atomic arrangements (environments) pertinent to our study. The letters in parentheses correspond to those used in Figs. 6 and 7 for the CNA signatures. Listed for each atomic environment the total number of nearest neighbors (#bonds) followed by a list of the corresponding CNA signatures with the number of times each occurs in parentheses. The information in this table corresponds to the ideal (perfect) structures.

Environment	# bonds	CNA(#)	CNA(#)	CNA(#)	CNA(#)	CNA(#)
fcc bulk (a)	12	421(12)				
fcc (100) surface (b)	8	421(4)	211(4)			
fcc (111) surface (c)	9	421(3)	311(6)			
fcc (111)-(100) edge (d)	7	421(2)	311(2)	211(3)		
fcc (111)-(111) edge (e)	7	421(1)	311(4)	200(2)		
truncated octahedron vertex[a] (corner) (f)	6	421(1)	311(2)	211(2)	200(1)	
icosahedral internal twinning plane (g)	12	422(6)	421(6)			
icosahedral spine[b] (h)	12	555(2)	422(10)			
icosahedral surface edge (i)	8	422(2)	322(2)	311(4)		
icosahedral central atom (j)	12	555(12)				
icosahedral surface vertex or decahedral axial vertex (k)	6	555(1)	322(5)			
truncated icosahedral vertex or decahedral notch vertex[c] (l)	7	422(1)	322(1)	311(2)	300(1)	200(2)
decahedral notch edge[d] (m)	10	422(2)	421(2)	311(4)	300(2)	
tetrahedral edge	6	311(4)	211(2)			
bcc bulk	14	666(6)	444(8)			

[a]A vertex atom such as one on a truncated octahedral cluster of fcc material at, for example, the intersection of a (111), a $(1\bar{1}1)$, and a (100) surface plane.

[b]An atom in the row of atoms on the line connecting the central atom of an icosahedral cluster and one of its surface vertex atoms. This signature also occurs for atoms on the axis of a decahedral cluster between the two axial vertex atoms.

[c]The removal of an icosahedral vertex atom leaves five new vertex atoms with this signature which had formerly been on an icosahedral edge. The vertex atom on a (notched) Marks' decahedron (see Fig. 1) at the intersection of two adjacent capping (111) planes at the inside corner of the notch has the same local environment.

[d]Atoms on the inside edge of a decahedral notch, between the two decahedral notch vertices.

APPENDIX A: COMMON NEIGHBOR ANALYSIS

We employ the method of common neighbor analysis[28] (CNA) to characterize local atomic environments within the clusters. We identify a given atom's nearest neighbors as simply those closer to it than an appropriately chosen distance r_c, which we take as 3.5 Å, midway between the nearest- and next-nearest-neighbor shells in fcc gold. Results from this analysis for these clusters are insensitive to the precise value of r_c. We speak of each pair of nearest-neighbor atoms as being ''bonded'' and being connected by a ''bond,'' but this merely denotes a geometrical relationship and not a chemical one.

CNA fundamentally operates by categorizing such bonds. Each of a bond's two atoms has a set of nearest neighbors; the intersection of those two sets comprises the neighbors that the two atoms have in common. CNA characterizes the bond by examining this set of common neighbors and specifying three numbers: (1) the total number of atoms in the set, (2) the total number of bonds between atoms in it, and (3) The number of bonds in its largest contiguously bonded subset. While in general a given CNA bond signature may correspond to more than one possible common-neighbor configuration, in practice this is not a problem in this study. Thus in a fcc bulk crystal, each nearest-neighbor pair shares four common neighbors, among those common neighbors two disjointed bonds are found (so that the longest chain of bonds has only one member). Thus the CNA signature of the bond is 421. Since all 12 of the bonds of each atom in a fcc crystal are the same, we say that the local environment of an atom with 12 nearest neighbors each of which has a 421 CNA signature is that of fcc bulk.

Similarly an atom in a hexagonal-close-packed bulk crystal (or equivalently one on a twinning plane in a fcc crystal) has six bonds with the 421 signature and six with a 422

signature. Table I lists the CNA signatures for some of the interesting atomic environments considered in this study. Note that classification of an atomic environment as described above is inherently conservative in the sense that if only one bond fails to match a possible signature, that signature is entirely rejected. In order to find configurations which are near to that of fcc bulk, for example, it is necessary to explicitly catalog any signatures one wants to characterize as having that property and track them separately.

APPENDIX B: CONFIGURATION/PROPERTY. PLOTS

The thermal evolution may be illustrated and summarized through the configuration/property (c/p) plots, shown in Figs. 10 and 11 for the Au_{146} and Au_{459} clusters, respectively. In these figures we show, for selected stages of the thermal evolution of the clusters [marked by letters corresponding to those denoted on the caloric curves, Figs. 1(b) and 1(c)], atomistic energetics and mobility characteristics (calculated per atom) superimposed on the corresponding atomic cluster configurations (an expanded color c/p plot for the Au_{459} can be found as Fig. 2 in Ref. 20).

In both figures we display in the left column atomic configurations, at the marked thermal stages, corresponding to the orientations of the Au_{146} and Au_{459} clusters shown in Fig. 1, viewed along the normal to the page. For both clusters we observe at low temperatures (L in Fig. 10, and L and A in Fig. 11) that the superimposed atomic potential energies (shaded according to the energy scales given at the top of the figures) ''trace'' the structural features of the clusters (truncated-decahedral for Au_{146} and fcc-TO$^+$ for Au_{459}), with edge and corner atoms characterized by lower binding energies (less negative values of the potential energy U,

shaded lighter) than those of facet and interior atoms. For the Au_{146} cluster we show also in the second column of Fig. 10 configuration/energy plots corresponding to a (top) view along the axis connecting the top and bottom vertex atoms of the decahedron (that is, a view obtained via a 90° rotation about the left-right x axis of the decahedron shown at the top left corner of the figure). Additionally, we display in the third column of Fig. 10 configuration/energy plots obtained via cutting of the cluster shown in the second column with a meridian (north-south) plane normal to the page followed by a 90° left rotation of the left half of the cluster, thus allowing a view of the cluster interior. The configuration/diffusion plots in the fourth and fifth columns of Fig. 10 correspond to the cluster configurations shown in the first and third columns, respectively. For the Au_{459} cluster the configuration/diffusion plots in the second column of Fig. 11 correspond to the cluster configuration shown in the first column, and those displayed in the third column correspond to configurations obtained from that shown in the second column through a meridian-planar cut followed by rotation as described above.

The structural transformations are evident from inspection of Figs. 10 and 11; see the c/p plots corresponding to stage C in Fig. 10 (Au_{146}) showing a m-$Dh \rightarrow Ih$ transformation with no indication for enhanced atomic diffusion, and those corresponding to stage C in Fig. 11 (Au_{459}). Moreover, from the configuration/diffusion plot shown in the third column of Fig. 11 (stage C), we observe that the transformed crystalline solid icosahedral part of the Au_{459} cluster is in equilibrium coexistence with a liquid (melted) part which does not wet the solid fraction [see also panel C in Fig. 3(c)]. Eventual melting of the clusters is observed in stages G (Fig. 10) and D (Fig. 11).

[1] W. Thomson, Philos. Mag. **42**, 448 (1871).

[2] P. Pawlow, Z. Phys. Chem. (Munich) **65**, 545 (1909).

[3] Ph. Buffat and J. P. Borel, Phys. Rev. A **13**, 2287 (1976).

[4] J. Bovin, R. Wallenbreg, and D. Smith, Nature (London) **47**, 317 (1985).

[5] S. Iijima, in *Microclusters*, edited by S. Sugano *et al.* (Springer, Berlin, 1987), p. 186.

[6] P. M. Ajayan and L. D. Marks, Phase Transit. **24-26**, 229 (1990); Phys. Rev. Lett. **60**, 585 (1988); **63**, 279 (1989).

[7] See review by R. S. Berry, T. L. Beck, H. L. Davis, and J. Jellinek in *Evolution of Size Effects in Chemical Dynamics*, edited by I. Prigogine and S. A. Rice [Adv. Chem. Phys. **70**, 75 (1988)], Pt. 2.

[8] J. Luo, U. Landman, and J. Jortner, in *Physics and Chemistry of Small Clusters*, edited by P. Jena, B. K. Rao, and S. N. Khanna (Plenum, New York, 1987), p. 201.

[9] T. Castro *et al.*, Surf. Sci. **234**, 43 (1990).

[10] F. Ercolessi, W. Andreoni, and E. Tosatti, Phys. Rev. Lett. **66**, 911 (1991).

[11] H.-P. Cheng and R. S. Berry, Phys. Rev. A **45**, 7969 (1992); R. S. Berry, in *Clusters of Atoms and Molecules*, edited by H. Haberland (Springer, Berlin, 1994), pp. 187–204.

[12] S. Valkealahti and M. Manninen, Comput. Mater. Sci. **1**, 123 (1993).

[13] T. P. Martin, U. Naher, H. Schaber, and U. Zimmerman, J. Chem. Phys. **100**, 2322 (1994).

[14] C. L. Cleveland, U. Landman, and W. D. Luedtke, J. Phys. Chem. **98**, 6272 (1994).

[15] O. H. Nielsen *et al.*, Europhys. Lett. **26**, 51 (1994).

[16] See the review by L. D. Marks, Rep. Prog. Phys. **57**, 603 (1994), and references therein.

[17] L. J. Lewis, P. Jensen, and J.-L. Barrat, Phys. Rev. B **56**, 2248 (1997).

[18] M. Schmidt, R. Kusche, W. Kronmuller, B. von Issendorft, and H. Haberland, Phys. Rev. Lett. **79**, 99 (1997).

[19] A. Rytkonen, S. Valkealahti, and M. Manninen, J. Chem. Phys. **106**, 1888 (1997); **108**, 5826 (1998).

[20] C. L. Cleveland, W. D. Luedtke, and U. Landman, Phys. Rev. Lett. **81**, 2036 (1998).

[21] M. Schmidt, R. Kusche, B. von Issendorft, and H. Haberland, Nature (London) **393**, 238 (1998).

[22] T. P. Martin, Phys. Rep. **95**, 167 (1983).

[23] J. F. Van der Veen *et al.*, in *Kinetics of Ordering at Surfaces*, edited by M. G. Lagally (Plenum, New York, 1990), p. 343; see also Ref. 10.

[24] (a) C. L. Cleveland, U. Landman, T. G. Schaaff, M. N. Shafigullin, P. W. Stephens, and R. L. Whetten, Phys. Rev. Lett. **79**, 1873 (1997); (b) R. L. Whetten, J. T. Khoury, M. M. Alvarez, S.

Murthy, I. Vezmar, Z. L. Wang, P. W. Stephens, C. L. Cleveland, W. D. Luedtke, and U. Landman, Adv. Mater. **5**, 428 (1996); (c) C. L. Cleveland *et al.*, Z. Phys. D **40**, 503 (1997).

[25] L. D. Marks, Philos. Mag. **49**, 81 (1984); J. Cryst. Growth **61**, 556 (1983).

[26] C. L. Cleveland and U. Landman, J. Chem. Phys. **94**, 7376 (1991).

[27] Atomic diffusion is calculated for atom i from the slope of $\bar{R}_i^2(\Delta t)/6 = \langle R_i^2(\Delta t, t_0) \rangle_{t_0}/6$, where $\langle \cdots \rangle_{t_0}$ denotes an average over time origins, t_0, and where $R_i^2(\Delta t, t_0) = [r_i(t_0 + \Delta t) - r_i(t_0)]^2$. Since an atom's mobility can change, we must restrict the span of time origins averaged together. We have chosen 30 ps as a time range that is relatively small compared with the rate at which an atom's mobility changes, but large enough to provide a significant degree of averaging for the diffusion estimate. When averaging is restricted to such short intervals, as it is in Figs. 4(a)–4(c) and for the atomic configuration/property plots of Figs. 10 and 11, we compensate for such limited time averaging by calculating D' assigned to time $\bar{t}$ from $D_i'(\bar{t}) = \langle R_i^2(\Delta t, t_0) \rangle_{t_0}/6\Delta t$, using $\Delta t = 60$ ps, and $\bar{t}$ is the average of all the time end points used in the calculation of $D_i'(\bar{t})$.

[28] D. Faken and H. Jonsson, Comput. Mater. Sci. **2**, 279 (1994).

[29] A. Guinier, *X-Ray Diffraction* (Freeman, San Francisco, 1963).

[30] A. Howie, Nature (London) **320**, 684 (1986).

[31] A. Williams, Appl. Phys. Lett. **50**, 1761 (1987).

[32] S. Iijima and T. Ichihashi, Phys. Rev. Lett. **56**, 616 (1986).

[33] D. J. Smith and L. D. Marks, J. Cryst. Growth **54**, 433 (1981); see, in particular, Fig. 9.